THE $N^{O}E$ DETECTOR FOR A LONG BASELINE NEUTRINO OSCILLATION EXPERIMENT

G.De Cataldo, L.De Benedictis, C.Favuzzi, P.Fusco, N.Giglietto, A.Rainò, M.N.Mazziotta, P.Spinelli
Dip. di Fisica dell'Università di Bari and INFN Sez. di Bari - Italy

A.Margiotta, M.Spurio
Dip. di Fisica dell' Università di Bologna and INFN Sez. di Bologna - Italy

A.Di Credico, A.Grillo, C.Gustavino, S.Mikheyev[1], E.Scapparone
INFN, Laboratori Nazionali del Gran Sasso, Assergi - Italy

P.Bernardini, G.Mancarella, D.Martello, A.Surdo
Dip. di Fisica dell' Università di Lecce and INFN Sez. di Lecce - Italy

R.A.Mukhamedshin, G.T.Zatsepin
Institute of Nuclear Research, Moscow, Russia

V.A.Smotryaev, I.S.Trostin
Institute of Theoretical and Experimental Physics, Moscow, Russia

K.V.Alexandrov, V.A.Chechin, A.P. Chubenko, A.D.Erlykin, F.F.Kayumov, S.K.Kotel'nikov, E.P.Kuznetsov, B.N.Lomonosov, G.I.Merzon, V.A.Ryabov, V.O.Tikhomirov, V.A.Tsarev
P.N.Lebedev Physical Institute, Moscow, Russia

A.M.Baranov, E.T.Gushchin, V.A.Kantserov, A.A.Semak, S.V.Somov
Moscow Engineering Physical Institute, Moscow, Russia

M.Ambrosio, C.Aramo[2], G.C.Barbarino[*], D.Campana, F.Guarino, A.Lauro, A.Ordine, G.Osteria, U.Rubizzo
Dip.di Scienze Fisiche dell' Università di Napoli and INFN Sez.di Napoli-Italy

S.Bussino, M.De Vincenzi[3], E.Lamanna
Dip. di Fisica dell' Università di Roma and INFN Sez. di Roma - Italy

G.V.Gavalian, R.L.Kavalov, M.P.Lorikian
Yerevan Physical Institute, Yerevan, Armenia

[*] Contact person
[1] also Institute of Nuclear Research, Russian Academy of Science, Moscow, Russia
[2] also Dip. di Fisica dell' Università di Catania and INFN Catania - Italy

[3]also Dip. di Fisica dell' Università di Roma III - Italy

We present the long baseline experiment (N^OE) at the Gran Sasso Laboratory for the measurement of neutrino masses looking for $\nu_\mu \to \nu_\tau$ and $\nu_\mu \to \nu_e$ oscillations.

1 Introduction

The philosophy of the N^OE detector design is to have oscillation sensitivity in two separate ways: by measuring a deficit of muons in apparent NC/CC ratio and by looking for the τ decay in $\nu_\mu \to \nu_\tau$ or for an electron excess in $\nu_\mu \to \nu_e$.

The major experimental hint for the long baseline ν oscillation search in the regime of low Δm^2 ($10^{-2} \div 10^{-3}$ eV^2) comes from the muon deficit observed by the Kamiokande [1] IMB [2] MACRO [5] and SOUDAN [6] experiments. At present the new SuperKamiokande experiment [3] [4] confirms the observed effect in Kamiokande data. Recent results from CHOOZ, a long baseline reactor neutrino experiment [7], show no evidence for neutrino oscillation in $\bar{\nu}_e$ disappearance mode, up to $\sin^2 2\theta > 0.18$ for large Δm^2.

Given the SuperKamiokande confirmation of the atmospheric neutrino anomaly and the negative CHOOZ result, a Long BaseLine (LBL) experiment has to fulfill the following requirements:

1. **The measurement of the parameter NC/CC**. This robust and unambiguos test is mandatory to investigate on the existence of a neutrino oscillation signal in LBL experiments. Morever in a scenario, never ruled out, in which a neutrino oscillates with large mixing angle and $\Delta m^2 \simeq 10^{-2} \div 10^{-3}$ eV^2 in a sterile neutrino ($\nu_\mu \to \nu_x$) the oscillation can be discovered only by measuring near and far ν_μCC spectra. There is no doubt that this measurement can be done only with a massive detector.

2. ν_τ **tagging**. If the oscillation signal is seen by measuring NC/CC ratio, the search for ν_τ appearence becomes a very important task. This search requires high detector performances.

   The appearance of τ's can be definitively detected in N^OE by observing a signal in several channels, each one corresponding to a different τ decay. The detection of oscillated events with the appearance method and the μ-deficit obtained studying the NC/CC ratio will allow a redundant oscillation signal measurement.

3. **Atmospheric neutrinos**. After the SuperKamiokande results, which suggest a possible shift of Δm^2 to smaller values, the interest for the

atmospheric neutrinos is raised up. It would be interesting, for a LBL experiment to test this effect using a massive detector based on a different technique with respect to the water Čerenkov detectors.

4. **Fast response**. If a beam from CERN to Gran Sasso will be available in the next years, a strong competition with American and Japanese experimental LBL programs is foreseen: at present, the 7 kton N^OE project can adequately compete with the 8 kton MINOS detector and with K2K.

According to the present oscillation scenario, the N^OE research program can be summarized in this way:

- Inclusive (NC/CC) ν_μ disappearance and direct ν_τ appearance by kinematical tau decay reconstruction.
- Investigation of $\nu_\mu \to \nu_e$ oscillation in a mixing angle region two orders of magnitude beyond the CHOOZ limit.
- Atmospheric neutrino studies.

Many efforts have been done to obtain a deeper understanding of the N^OE detector in terms of performances, granularity and cost in order to achieve the described physics goals.

The recent N^OE evolution towards a more sophisticated layout devoted to ν_τ appearance is presented in detail in this report. In order to improve the ν_τ search, the apparatus has been implemented with Transition Radiation Detector (TRD) interleaved between calorimetric modules (CAL). The combination of TRD and CAL information strongly enforces e, μ, and π identification, thus opening, besides $\tau \to \mu$, new tau decay channels: $\tau \to \pi$ and $\tau \to e$ with very clean signatures. The last one is particularly favoured due to the low background (residual ν_e beam). The good electron identification in the TRD target and the low π^0 background allow to obtain high $\sin^2 2\theta$ sensitivity in the $\nu_\mu \to \nu_e$ oscillation channel, thus considerably enlarging the region investigated by the CHOOZ reactor experiment. Both TRD and CAL will be extensively discussed.

The TRD is an evolution of that now operating in the MACRO detector at Gran Sasso. The performances of this kind of detector are well known and the technique is largely proven. In order to contain the cost of the calorimeter as much as possible, different options have been examined and the performances compared as well. The project is still in progress, in particular as far as the electronic read out, trigger, data acquisition and detector optimization are concerned. It should be stressed that this massive detector is based on proven technology which guarantees complementarity to the approved ICARUS experiment.

2 Detector design

The low ν-beam luminosity at long distance (beam luminosity decreases as $1/L^2$) implies that a long baseline detector must be very massive and have a diffuse target. Unlike the case of short baseline experiments these constraints imply a detector in where parts should be, at the same time, target, tracker, calorimeter, and μ-detector.

Oscillation tests can be grouped in two classes:

1. Inclusive measurements:
   - ν_μ disappearance: comparing the fluxes measured near the accelerator and in the far detector, the presence of a μ-deficit at long distance can be tested.
   - Measurement of the ratio of events without muon track (appearing NC events) with respect to those with a muon track (appearing ν_μ CC events).
2. Exclusive measurements:
   - Search for ν_τ and/or ν_e appearance. This analysis can be performed on an event by event basis, taking advantage of both the spatial and the topological event reconstruction. A detector devoted mainly to this measurement should have very high granularity as well as good particle identification capability. A beam monitor, identifying the residual ν_e beam background, could be also very useful for this kind of analysis.

Inclusive measurements require only μ identification in the detector and do not need event reconstruction. On the contrary, exclusive measurements require enough granularity to permit the separation between CC interactions with or without τ's in the final state when $\nu_\mu \to \nu_\tau$ oscillation occurs. Such a discrimination is based on the measurement of the missing momentum in the plane orthogonal to the ν-beam direction, on the angular correlation between missing momentum, outgoing lepton (pion) and hadronic jet directions as well. In ν_τ CC interactions, the missing momentum is mainly due to the neutrino(s) coming out from tau decay.

In $\nu_\mu \to \nu_e$ oscillation an excess of electrons will be looked for. Also in this oscillation channel the granularity allows to separate the genuine signal from NC with π^0 events. Hence, general requirements for an adequate detector performing such exclusive measurements are the following:

- The mass in a large fiducial volume must be enough to contain the events inside the detector in order to have good sensitivity limits.
- e, μ, π^0, $\pi^{\pm}$ discrimination.
- Fine topological readout to determine the shower axis and to allow electron - pion discrimination by the analysis of lateral and longitudinal shower profiles.
- Good kinematical reconstruction in terms of energy and angle of final prongs.

LBL experiments should be able to perform more than one oscillation test simultaneously. Moreover, when a large signal (atmospheric anomaly) is present, a detector with a good energy resolution can easily follow the oscillation modulation, as a function of L/E (E varying while L, the distance from the accelerator to the detector is fixed).

A good compromise between mass and granularity allows to perform all these measurements.

3 The N^OE Detector

According to the previous conceptual considerations, the essential elements of the N^OE detector are a massive, fine grain 4.3 kton calorimeter (CAL) interleaved with "lighter" Transition Radiation Detector (TRD) modules for a total TRD mass of 2.4 kton. Both TRD and CAL modules, joined together, form the Basic Module (BM) of the N^OE detector (Fig. 1). The whole 7 kton N^OE detector is made of twelve subsequent BM (Fig. 2).

In this report we show that also in LBL experiments two subdetectors can be used, thus improving the detector performances. Particle identification in TRD and CAL, electron and hadron energy measurements in CAL and muon energy measurement in TRD, are the high quality features of this new and unique LBL detector. Background reduction is increased, allowing easy appearance oscillation signatures. In addition lighter TRD and heavier CAL detector-target, exploiting their different properties, can be addressed to independent classes of events, in particular recovering the quasi elastic and resonant interactions.

Combining the information coming from both subdetectors (TRD and CAL) the discrimination between electrons, muons and pions is strongly improved, thus opening, besides $\tau \rightarrow \mu\nu\nu$, the study of other τ decay channels.

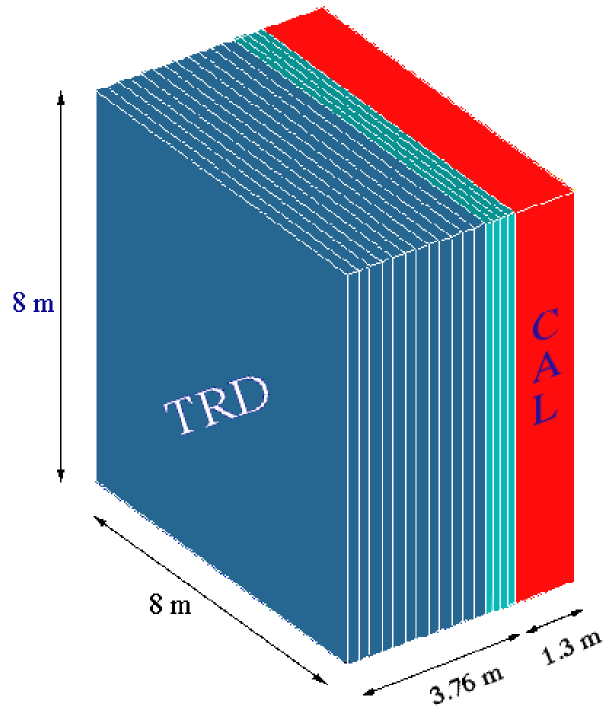

Figure 1: The Basic Module of the N^OE detector

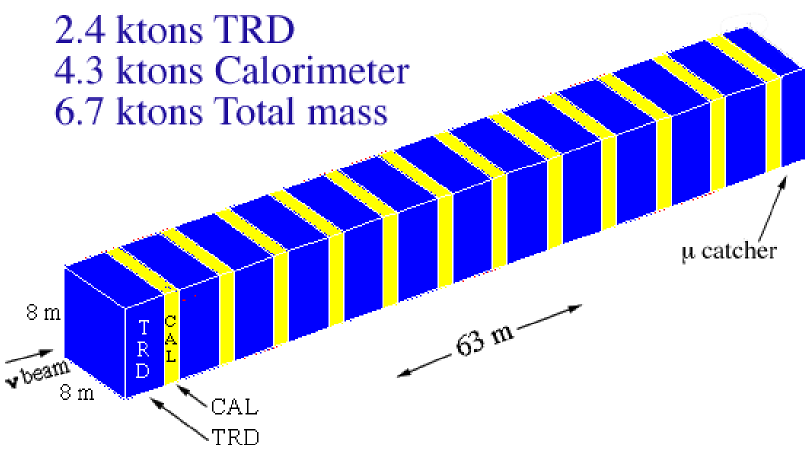

Figure 2: Schematic view of the N^OE detector

The TRD radiators, interleaved with multiple graphite layers, allow to measure quasi elastic events, reducing at a level as low as possible the nuclear reinteraction effects.

Since the transition radiation is detected by many layers of proportional tubes, the muon energy can be determined by multiple measurements of the energy loss dE/dx, once a muon track is recognized in the calorimeter. The advantage of such a "distributed muon detector" is the capability to measure the muon energy even for muon tracks exiting the apparatus from the side walls, thus increasing the detector acceptance.

Based on the same principle, a muon catcher to measure the muon energy when the neutrino interaction occurs in the last TRD or CAL target, is placed at the end of the detector.

The contribution to the total cost of TRD and CAL subdetector has to be cleverly shared in order to keep the detector cost as low as possible. In general, for a given mass, this layout does not introduce any additional cost with respect to a single subdetector module. Being the TRD technique well known and proven, the cost can be easily evaluated. A large volume TRD built for the MACRO detector has been extensively experimented at Gran Sasso, thus ensuring to the present collaboration the suitable expertise.

As far as the calorimeter is concerned, different designs have to be carefully examined, in order to compare cost and feasibility without loosing the calorimetric performances.

4 The N^OE TRD

The main task of the TRD subdetector (combined with CAL) is to provide a very clean electron identification, followed by an energy measurement in the calorimeter. Besides ν_e appearance search, new τ decay channels can be opened by looking at e and π tau decays. Due to the low electron background coming from the residual ν_e beam (1% ν_μ), the $\tau \to e\nu\nu$ channel is particularly favoured. In fact, even without event reconstruction, the electron signal overcomes the background when the atmospheric parameters are considered.

A second fundamental task fulfilled by a TRD subdetector is the energy measurement of the muon generated in ν_μCC and ν_τCC interactions.

Since muon tracks cross many layers of TRD proportional tubes, the long pathlength in the gas allows to obtain the μ energy, through multiple dE/dx measurements, with a resolution comparable to that achieved by using magnetic field technique. The described method is not expensive, it does not need electric power, magnetic coil and heat dissipation. It can benefit of the low cost TRD subdetector that, at the same time, is able to fulfill two important

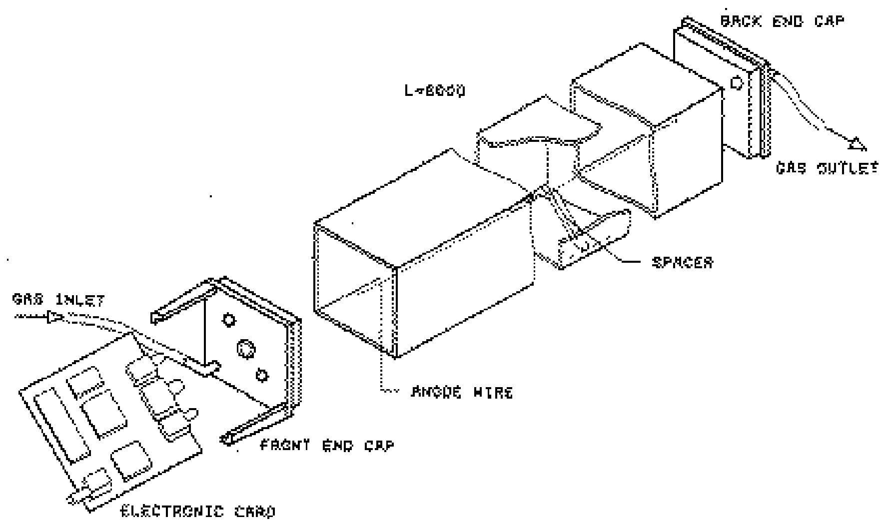

Figure 3: Tube layout.

tasks: e and π identification (together with the calorimeter) and muon energy measurement.

4.1 General description

The TRD module consists of 32 vertical layers of 8 $\times$ 8 m^2 surface area, each made of a polyethylene foam radiator ($\rho \sim 100$ mg/cm^3) and a group of 256 proportional tubes. The tubes have square cross section (3 $\times$ 3 cm^2) thus ensuring a uniform thickness detection layer (see Fig. 3).

The layers are alternatively positioned with the tube axis along the x and y directions to allow spatial reconstruction of charged tracks.

The total number of tubes inside a module is 8192.

A graphite wall of 5 cm thickness is set in front of each of the first 24 layers of the TRD acting as a 174 ton target for the ν_e, ν_τ interactions. The total length is about 3.76 m.

The last target wall is followed by eight TRD layers (as shown in Fig. 4), that still provide an optimal identification of the secondary particles. The total mass of the 12 basic TRD modules (including the foam and the tube materials) is about 2.4 kton. Each target wall corresponds to 0.25 X_0 while the entire TRD basic module corresponds to about 7 X_0 and 3.5 λ_I.

A cost saving option, in which polyethylene instead of graphyte is used as target has also been considered: in this case each target would correspond to

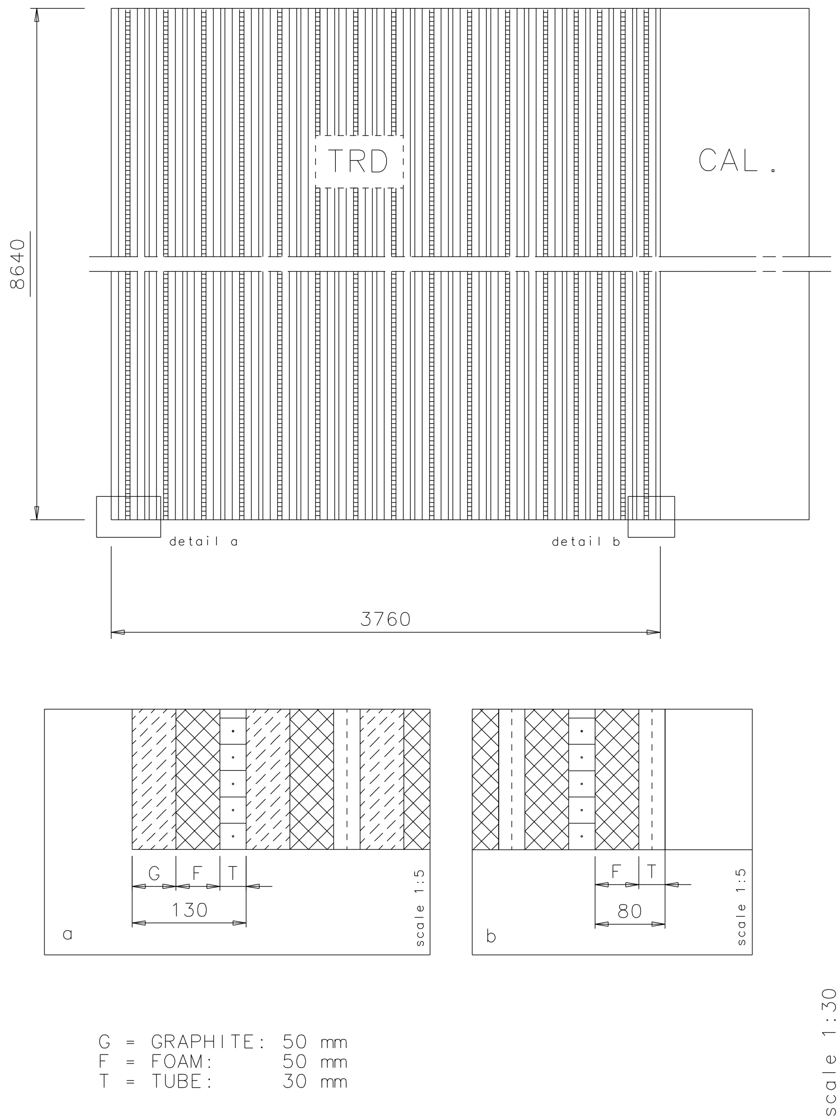

Figure 4: TRD layout.

0.1 X_0 while the entire module would correspond to about 3 X_0 and 1.8 λ_I. The total mass would be, in this case, reduced to 1.2 kton.

In order to convert efficiently the TR photons inside a tube of 3 $\times$ 3 cm^2 cross section, we intend to try either an Ar (60%) - Xe (30%) - CO_2 (10%) mixture we already tested in the MACRO TRD, or a Ar (80%) - CO_2 (20%), which is less efficient, but less expensive.

In Fig. 5 a Monte Carlo simulation of the pion contamination versus the number of TRD layers in the above proposed setup with the two possible gas mixtures is shown. This simulation is in agreement with the MACRO TRD results [12,13] indicated in the figure as check point.

The solution of spreading a low mass density target along the first 24 layers has been adopted for different reasons:

- the radiation length along the track of the produced electron is reduced (3.5 X_0 on average), so that it can be identified in several layers without the presence of secondary tracks from the e.m. shower. Fig. 5 shows that the pion contamination, even with a few layers, is of the order of a few percent (about 0.1 % with ten layers).

  It is also possible to give an estimate of the electron momentum in the range $0.5 \div 5$ GeV/c using the peculiar increase of the TR yield versus the γ Lorentz factor as we have done in the MACRO TRD for ultrarelativistic muons (Fig. 6). This possibility can be interesting when the electron is produced near the detector edges and misses the calorimeter.

- with a diluted target the density of secondary tracks near the production vertex is reduced thus allowing a better multiplicity recognition and space reconstruction of the event.

- the presence of proportional tube planes, inside the low X_0 target, lets a reasonable fraction of neutral pions (gammas) to travel for a few detecting layers without conversion. The lack of fired tubes near the vertex discriminates π^0 against electron induced showers starting from the interaction vertex. Fig. 7 shows the fraction of π^0 (gammas) which do not convert in TRD layers, versus the progressive layer number for graphite, polyethylene and aluminum for comparison. For example, 65% of π_0 do not convert before the third layer in graphite.

- one interaction length along the tracks of charged pions corresponds to 8 layers. Hence it is possible to identify pions as m.i.p.'s in several TRD layers before they interact.

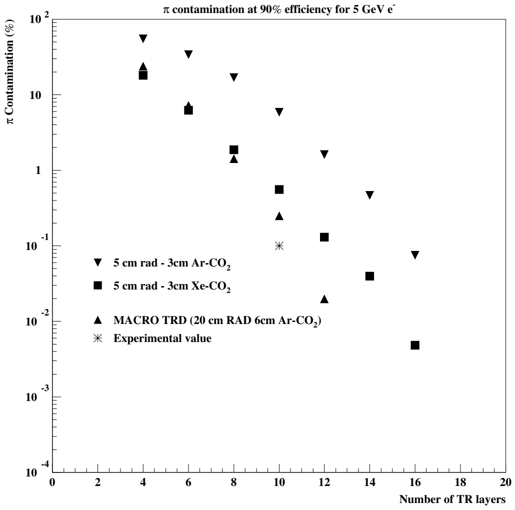

Figure 5: Pion contamination versus the number of crossed TRD planes (⋆ experimental MACRO values)

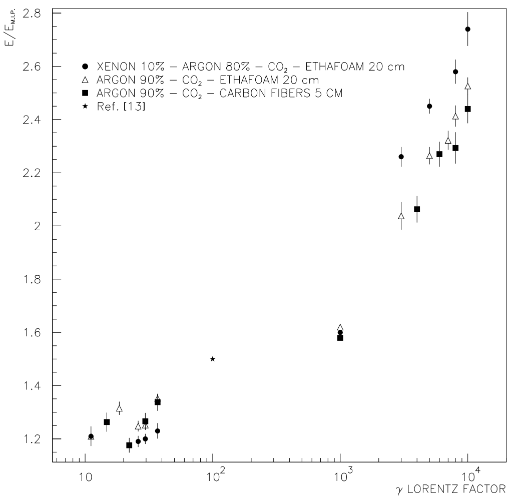

Figure 6: Energy deposited in TRD vs gamma Lorentz factor.

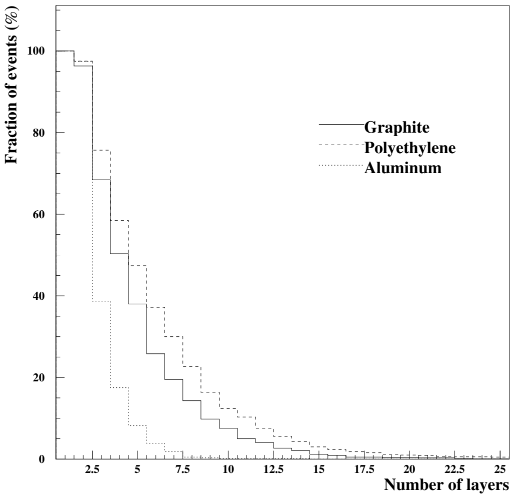

Figure 7: Fraction of π^0s that do not leave any signal in the TRD layers versus the progressive number of layers.

These considerations lead to conclude that the TRD has the ideal features for a powerful search of τ's decaying in electron and pion.

4.2 Proportional tube characteristics and performances

The proportional tubes used, like the MACRO TRD ones, are polystyrene extruded profiles of 0.9 mm thickness, but have a smaller cross section, 3×3 cm^2. This material is a carbon hydrogenate compound, has low density (1.1 g/cm^3) and is transparent to soft X-rays ($10 \div 20$ keV) which are produced by the foam radiators when crossed by electrons above 0.5 GeV/c momentum. The tube wall absorption at the transition radiation peak (11 keV) is only 18%. In addition this material ensures good mechanical stiffness and reduced gas permeability. In fact the MACRO TRD has been mounted simply piling up tubes and radiators without intermediate mechanical frames.

The tubes are internally coated with graphite paint and grounded, while the anodic central wire is set to positive high voltage. This wire is 100 μm thick and is positioned along the tube axis by X-shaped plastic spacers. The end-caps are equipped with gas inlet and outlet, and one of them holds the front-end electronic card, which is directly plugged to a pin soldered to the anodic wire.

The electronic channel consists of a preamplifier based on a BFR 92

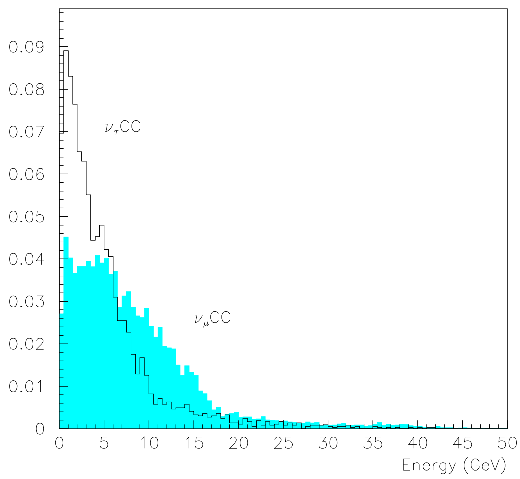

Figure 8: Expected muon spectrum.

high frequency transistor and a pair of cascade-connected amplifiers CLC505. With this configuration a 5.9 keV photon induced signal is formed to 20 ns F.W.H.M. [14].

5 Muon energy measurement

The TRD proportional tubes can be used to measure the muon energy in the range 1÷25 GeV/c, if this particle is identified as a clean non interacting track in any adjacent calorimeter module. This energy range nicely matches the expected muon spectrum, shown in Fig. 8.

As it is typically done to discriminate hadrons up to 100 GeV/c momentum using multiple dE/dx measurements in TPCs or proportional chambers, the ionization energy released inside the tubes must be carefully analysed by ADCs. In the EPI [15] detector (128 Ar gas samples each of 6 cm depth) the achieved ionization energy resolution was ±3%, thus allowing to separate pions from protons at 100 GeV/c, while in the ALEPH TPC [16], the resolution was about ±4.5% with 150 ÷ 300 samples, but using tracks in argon of much shorter lengths (of the order of 1.5 m).

From an inspection on the Bethe-Block dependence of the specific energy loss (ϵ=dE/dx) on the muon energy (Fig. 9), it turns out that, in order to achieve an energy resolution $\Delta E_\mu/E_\mu$ of about ±20 %, the ionization energy resolution $\Delta\epsilon/\epsilon$ measurement must be pushed to ±3% in the range 1 ÷ 10 GeV/c, and to ±1÷2% in the range 10÷20 GeV/c. Therefore the instrumental

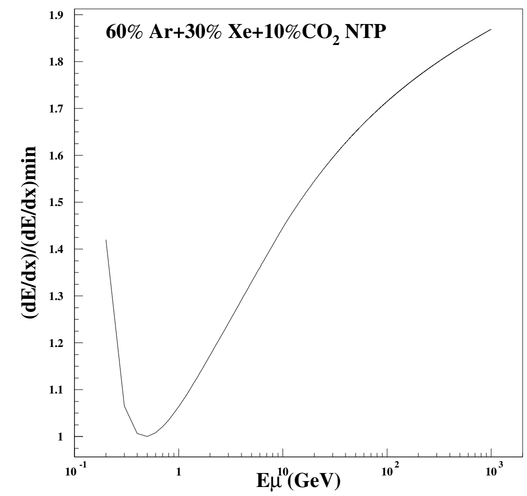

Figure 9: dE/dx in Argon - Xe - CO_2 gas mixture.

stability has to be taken within ±1%. In MACRO TRD this result has been obtained using a ^{55}Fe source.

Similar resolutions were achieved both by Ludlam [17] and in recent tests made at BNL on large volume "time expansion proportional chambers" [18,19], where the length of the tracks crossing the gas mixture was of the order of 20÷30 cm. FADCs were used to sample the dE/dx. A frequency of at least 41 MHz was used to sample the signals (formed at about 70 ns) in time bins of 24 ns, corresponding to about 0.5 mm track length.

It has been reported [19] that 4÷5 bits are enough to analyse the energy clusters inside the time bins. A simple truncated mean procedure on the cluster pulse height should yield ionization energy resolution of about 3 % per 1 m tracks in the Argon/Xenon mixtures. With this readout, the energy of a muon track crossing more than a basic module would be measured with accuracy even better than ±20 %, as shown in Fig. 10. Here these results are shown at various $\Delta\epsilon/\epsilon$ or track length for the Ar-Xe mixture. The asymmetry of the widths of the energy resolution ($\sigma_{LEFT} < \sigma_{RIGHT}$) is due to the logarithmic dependence of dE/dx on energy.

5.1 Experimental tests on proportional tubes with cosmic rays

In order to test the capability of the electronic channels to reach the ionization energy resolutions quoted above, a 1 m long proportional tube of 3×3 cm^2 cross section has been prepared, equipped with a card built according to the

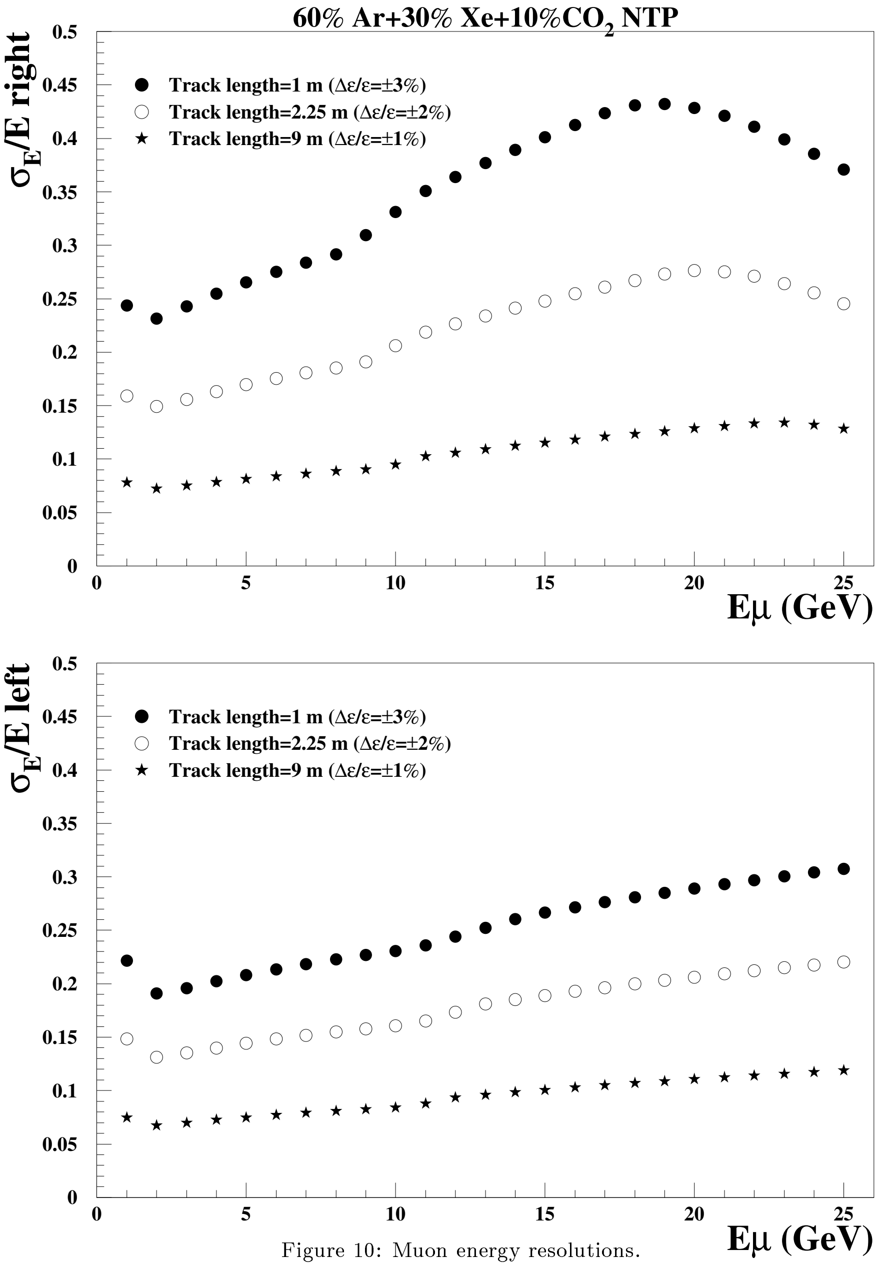

Figure 10: Muon energy resolutions.

proposed electronics layout. The tube with an Ar-Carbon dioxide mixture (80%-20%) has been placed between two scintillator rods of the same size acting as a telescope for cosmic rays. The signal gated by the telescope was analysed by a digital scope Le Croy 9361 of 500 MS/sec resolution and 5000 tracks were recorded. The typical signal shape consisted of several peaks due to clusters of ionization resolved by the electronic readout; in Fig. 11 (upper part) a typical signal of 1 μs width is shown. In order to reproduce the same signal sampling conditions as those of [18,19] the signal has been analysed by a software procedure using time slots of 24 ns corresponding to the effect of a 41 MHz FADC, after cutting the noise at 20 mV level (Fig 11 lower part).

Thirtytwo different tracks have been grouped to simulate, as usually done by other authors [17,18,19], a unique track corresponding to about 1 m gas length, and a cut on the highest 50% values, which removes them from the total sample, has been applied to the time slots contents (truncated mean procedure). Fig. 12 shows the distributions of these mean values obtained from a group of 150 "one-meter tracks" each one built as explained above. The FWHM of the distribution which is fitted by a gaussian is still fairly consistent with the expected resolution of $\pm$ 3% for one meter tracks. The discrepancy is mainly due to cosmic rays muon momentum spread.

5.2 Atmospheric neutrino tagging

The fast timing of the calorimeter allows to determine the direction of the atmospheric neutrino induced muons.

In order to tag the same class of events also in the TRD, all TRD module sides are enclosed in scintillator planes. The TRD module coverage is ensured by the adoption of scintillator strips of about 8 m length laid on the four sides without dead zones. The width of the strips is foreseen to be 6 cm, while the thickness would be 1 cm. These strips would be carved for the whole length by four channels on both faces, where four WLS fibers 2 mm thick will be placed. The photons will be in this case collected independently by these two groups of 4 fibers and sent to two independent PMTs. The coincidence of the two signals will be used as marker of an external crossing muon. The strip signal can be OR-ed in groups of 32 in order to give both a trigger and a timing signal for muons impinging on the TRD. For each TRD module there would be two layers of 256 strips each. For the whole apparatus the total number of strips would be 6144.

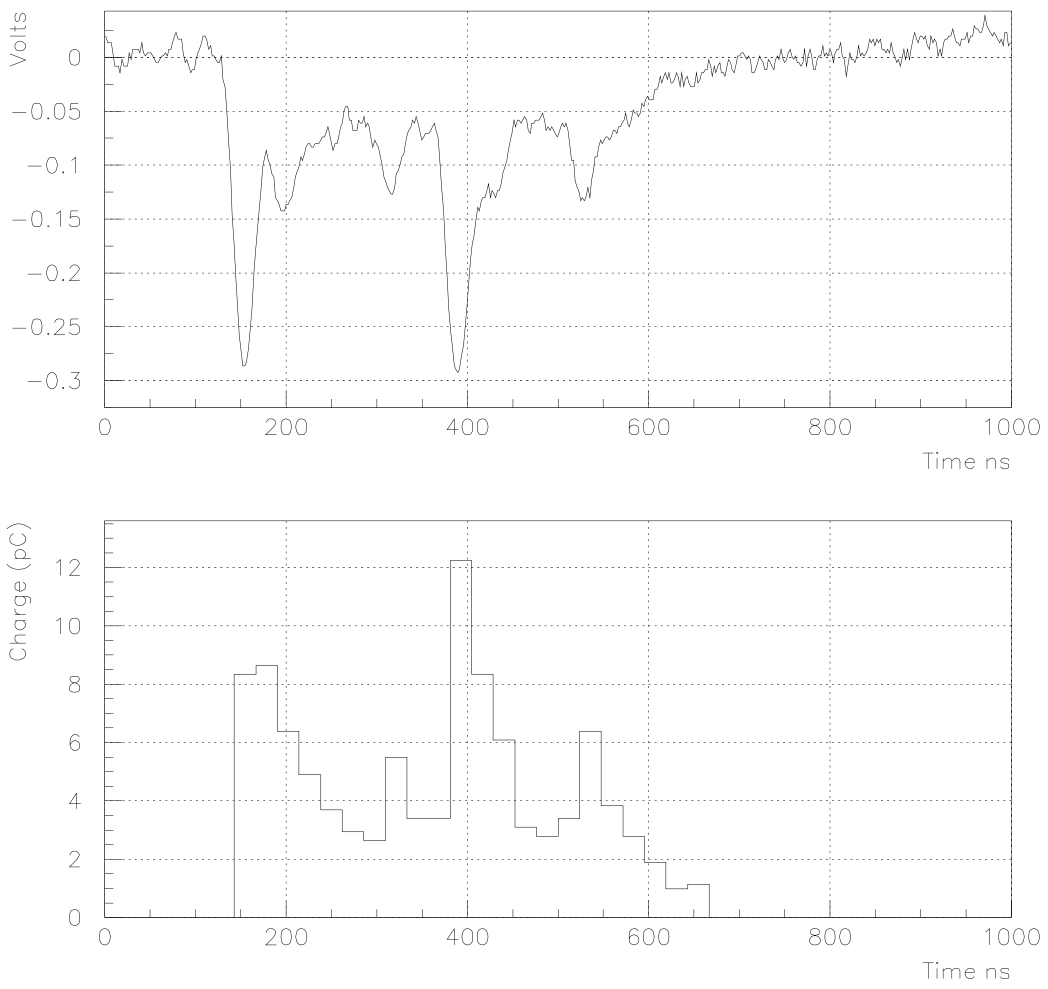

Figure 11: Upper part: typical signal shape. Lower part: result of the sampling procedure.

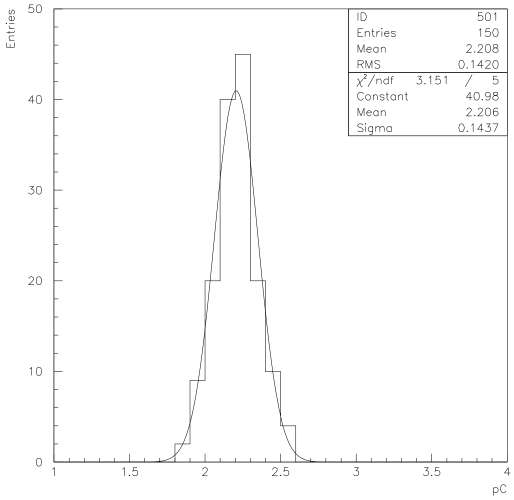

Figure 12: Average dE/dx for cosmic ray muons (pC).

5.3 The muon catcher

In order to measure the muon energy when the neutrino interactions occur in the last TRD and CAL targets, a muon catcher consisting of 32 layers of proportional tubes, equivalent to a TRD basic module is placed at the end of the $N^{O}E$ detector as shown in Fig. 2.

In this very small fraction of events the muon energy resolution corresponds to the 1 m length curve shown in Fig. 10.

6 The $N^{O}E$ calorimeter

The active part and the absorber of the calorimeter contribute to a significant fraction of the total cost of the $N^{O}E$ detector. Therefore different calorimeter layouts, based on the use of scintillation counters, must be carefully examined. In particular, a sampling iron calorimeter based on scintillating fibers or solid scintillator strips will be described. Features as light yield, resolutions, reliability and mechanical feasibility will contribute to the final choice.

The calorimeter design must fulfill the following requirements:

- The total mass of the calorimetric modules is $\sim$ 360 tons, in order to reach a total $N^{O}E$ mass of $\sim$ 7 ktons.
- The sampling must be $1 \div 1.5$ radiation length in order to achieve a good resolution.

Cell (cm^2)	**Fe (cm)**	**layers**	λ_I	X_0	$fibers, \lambda_I, X_0$ (number/cell)			**elec. chan.**
4×4	1.4	12x+12y	5.0	38	28	0.21	1.6	115200
5×5	1.5	10x+10y	5.1	37	44	0.26	1.8	76800
6×6	2.1	8x+8y	5.1	38	64	0.32	2.4	51200

Table 1: Main features of calorimetric bars

- The module must be as short as possible in order to gain acceptance, fiducial volume and save experimental hall space.

6.1 Crossed Fiber-Bars option (C.F.B.)

A preliminary calorimeter set up has been described in the letter of intent submitted to the Gran Sasso Committee in the occasion of a call for long baseline neutrino experiment proposals [8].

At that time the N^OE detector was composed by calorimetric bars with scintillating fibers and iron ore as active part and radiator respectively. The calorimetric technique of embedding scintillating fibers into the absorber has been developed in the past years and recently used in CHORUS [20] and KLOE [21] experiments. The calorimeter described in the following is an evolution of this technique addressed to massive detectors. In the previous letter of intent the basic calorimetric element was made by an 8 m long bar having iron ore and scintillating fibers suitably distributed in the bar and parallel to its axis. The whole detector was made by many alternate planes of crossed calorimetric bars (Fig. 6.1) [9,10].

A calorimetric bar consists of a number of logical cells with square cross section; the iron/iron-ore volume ratio is 0.3. In Table 1 the main features of the calorimeter in three different cell size hypotheses are shown. The total number of X and Y channels has been calculated assuming a two ended read out for each bar.

Fig. 14 shows the percentage of the active part (scintillator) crossed by a minimum ionizing particle (muon) going through the calorimeter.

At present the latest production developments of 2 mm diameter scintillating fibers leads to an attenuation length $\lambda = 4.5$ m (Fig. 15) and to an increase in light yield of 10-15 %. These figures allow to build 8 m long bars. Further investigations to improve fiber features are in progress.

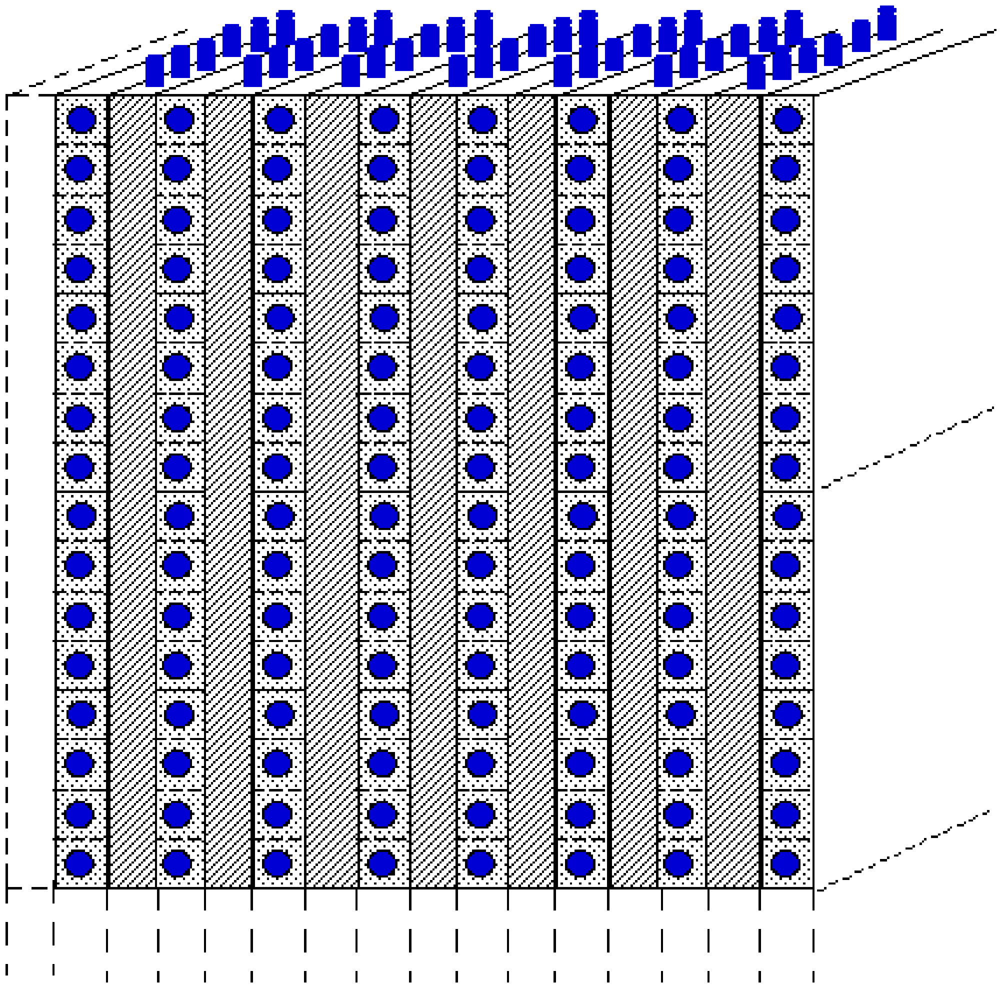

Figure 13: Details of the $N^{O}E$ calorimeter

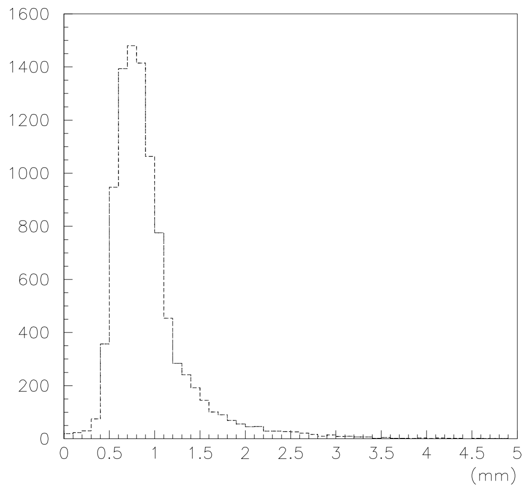

Figure 14: Thickness of scintillator crossed per cm of calorimeter by a minimum ionizing particle (muon)

$\%Fe$ (Weight)	Xo cm	λ_I cm	$<\rho>$ g/cm^3	$<Z>$	E_c MeV
70	5.6	44.5	3.0	15.2	37.

Table 2: Main features of the iron ore (hematite).

In a very simple and well proven way, for each calorimetric X,Y cells, all fibers are grouped together at each side of the calorimetric bar, then sent to single or multipixel photodetector.

Concerning the absorber, the iron ore has the following advantages:

1. it is practically cost free.

2. the radiopurity.

Fig. 16 shows the radioactivity spectrum of an iron ore sample. It can be inferred from the figure that iron ore acts as a screen against natural rock radioactivity and does not present any significant radioactive line above 700 keV. The very low background level leads to a low single counting rate particularly suitable to implement soft triggers for atmospheric neutrino events.

The main features of the iron ore absorber are shown in Table 2.

The extreme modularity of the N^OE calorimeter allows to assemble the detector outside the gallery, greatly improving the construction efficiency.

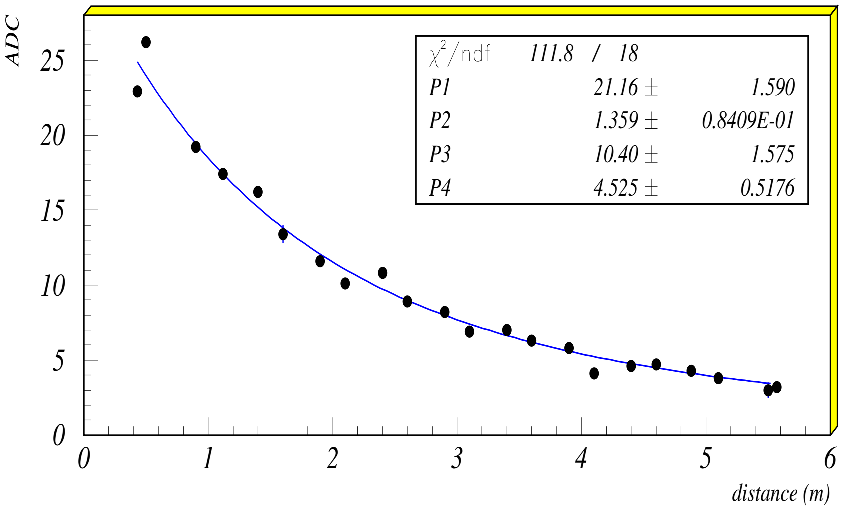

Figure 15: Experimental measurement of the fiber attenuation length

It is worth noting that the intrinsic granularity of the proposed calorimeter is very high: the average distance between the fibers inside the absorber is of the order of 3 mm.

6.2 Crossed Fiber-Planes option (C.F.P.)

A detail of the detector is shown in Fig. 17 [11]. In particular in Fig. 18 an 1/1 view of a calorimeter detail is shown.

Very thin iron sheets ($\sim$ 2 mm) provide the mechanical support for two planes of fibers embedded into the absorber. Fiber planes are positioned at both sides of the iron sheet, rotated 90° one with respect to the other. Each plane consists of self-supporting slabs made of extruded iron ore and recycled plastic. The 6.5 mm thin slab is made of two identical profiles which provide the fiber housing (Fig. 19).

The iron sheets are hung to a supporting mechanical structure. The general features of this calorimeter are shown in Table 3.

Such a layout allows a very fine sampling in the two views, which improves the accuracy of the shower axis determination. Moreover each pattern element is seen at the same time in the X and Y projections. With respect to the previous option the fiber density is unchanged, therefore half of the fibers are X (and half Y) oriented, thus doubling the read out channels. Table 4 shows the

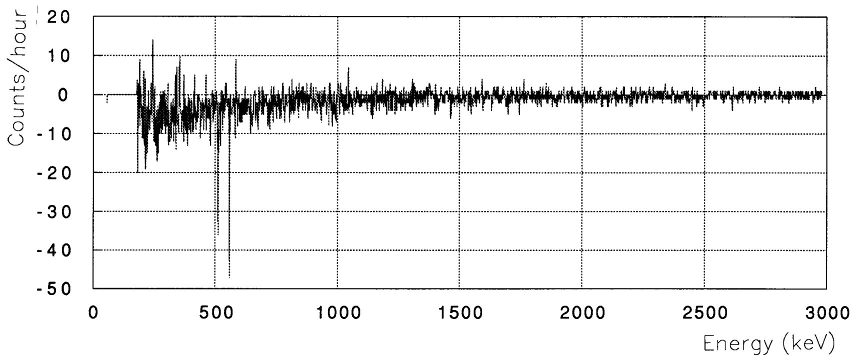

Figure 16: The radioactivity spectrum of an iron ore sample, after the subtraction of the environmental radioactivity.

$\%Fe$ (Weight)	Xo cm	λ_I cm	$<\rho>$ g/cm^3	$<Z>$	E_c MeV
72.4	5.5	45	3	21	27.4

Table 3: Average features of the calorimeter absorber.

main parameters of this calorimeter layout. The total number of XY channels has been calculated assuming two ended read out for each calorimetric cell.

The plastic and iron ore extrusion has been extensively developed and tested by two different factories that manufactured very high quality products with a density up to $\rho = 3.6$ g/cm^3 (see Fig. 20).

The additional cost of the extruded plastic and iron ore slab, only partially compensated for thinner iron sheet, is the major drawback of this solution.

6.3 Crossed Scintillator Strip option (C.S.S.)

Recently the interest towards extruded scintillator strips with wavelength shifter rods or fibers (WLS) has been rising and such devices have already been employed [24,25,26] (among others, also by some N^OE collaborators).

Light produced by the passage of particles through the strip may be captured inside a WLS fiber. The fiber re-emits the light isotropically and some of that will be transmitted out to the photodetector. The device is simple, robust and not expensive. Moreover, the extrusion reduces the manpower required for assembly. These considerations lead to the iron sampling calorimeter shown in Fig. 21. In the N^OE calorimeter all extrusion strips can be 8 m long arranged

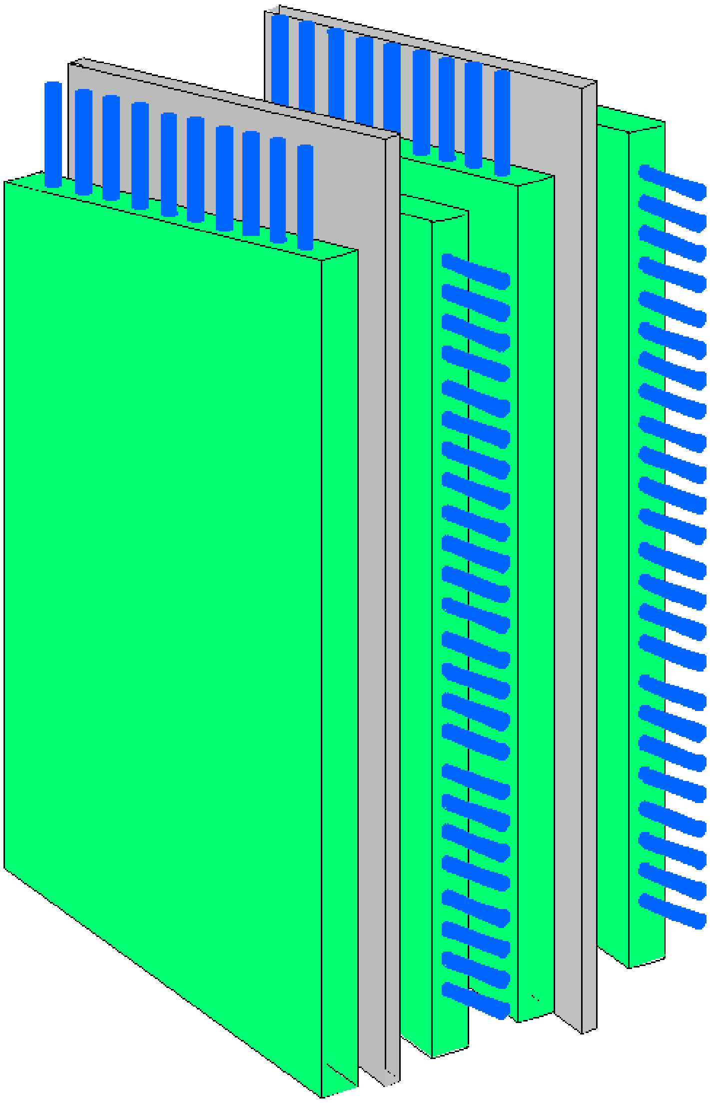

Figure 17: $N^{O}E$ calorimeter details (fibers, absorber and mechanical supports)

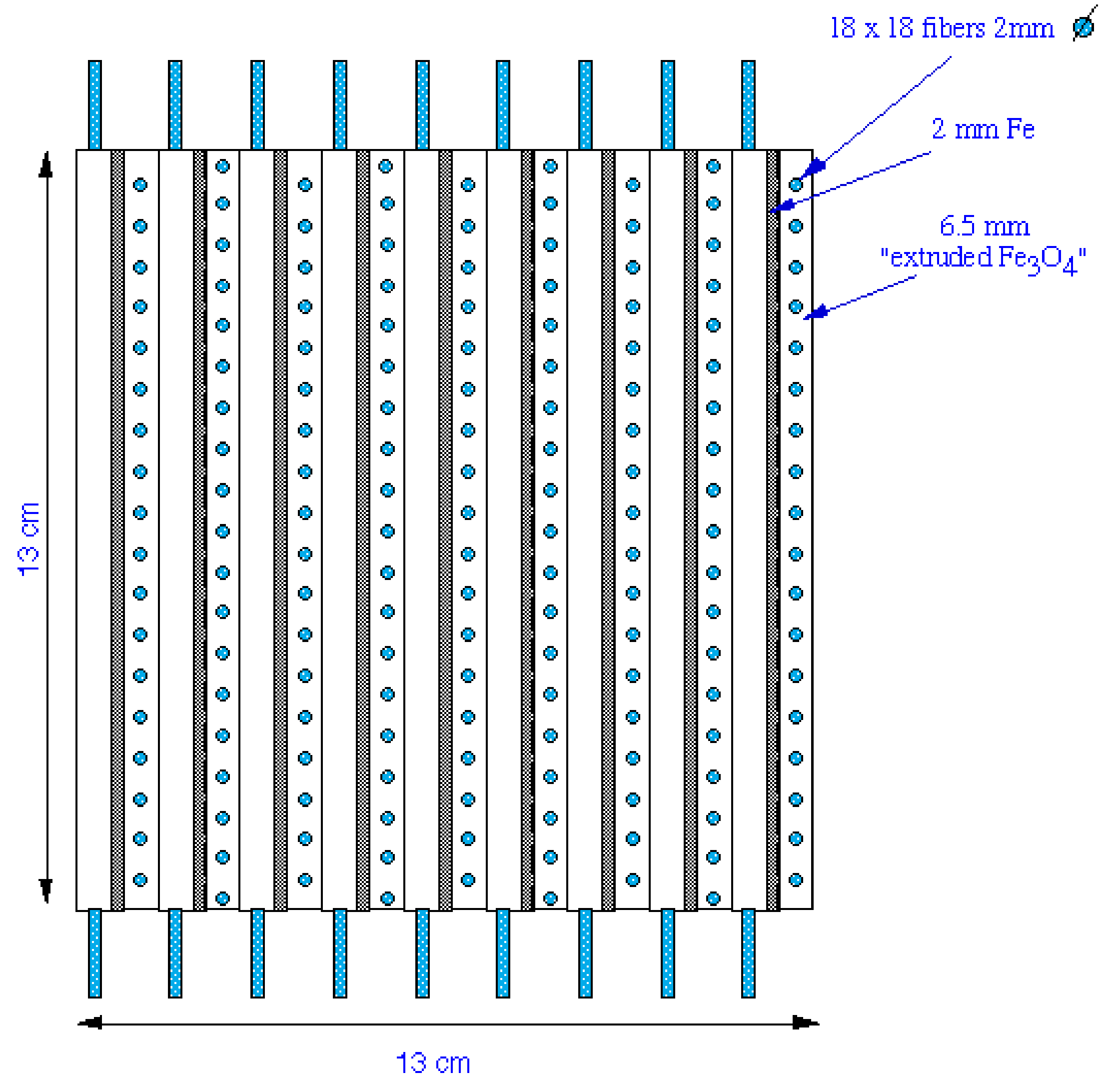

Figure 18: N^OE calorimeter details (fibers, absorber and mechanical supports)

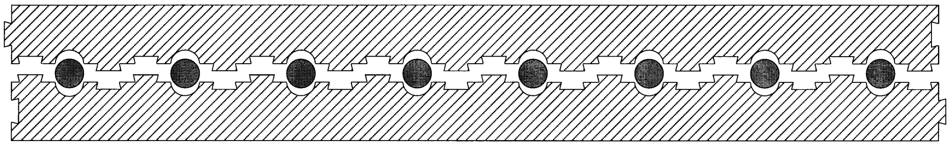

Figure 19: Self-supporting fiber housing

Cell ($\mathbf{cm^2}$)	**layers**	λ_I **tot.**	X_0**tot.**	$fibers, \lambda_I, X_0/cell$			**elec. chan.**
4×4	60 (xy)	4.2	29	14	0.14	.97	288000
5×5	48 (xy)	4.3	29	22	0.18	1.2	184320
6×6	40 (xy)	4.2	28	32	0.21	1.4	128000

Table 4: Main calorimeter features in the Crossed Fiber-Planes option

in X,Y planes faced to the iron slab absorber.

The number of total X,Y channels has been calculated assuming two ended read out for each strip. The principal disadvantage of the scintillating strips with WLS fibers is the light yield strongly suppressed by the light capture probability in the fiber. Many tests have to be done to optimize the strip dimension and the fiber diameter as well as the scintillator chemical composition in order to collect enough photoelectrons to achieve good efficiency and resolution. The main calorimeter parameters are reported in Table 5.

Cell ($\mathbf{cm^2}$)	**Fe** **(cm)**	**layers**	λ_I	X_0	$\lambda_I, X_0/cell$		**elec. chan.**
1×4	1.5	23x+23y	4.6	41	.1	.89	220800
1×2	1.5	23x+23y	4.6	41	.1	.89	445600

Table 5: Main calorimeter features in the Crossed Scintillator Strip option

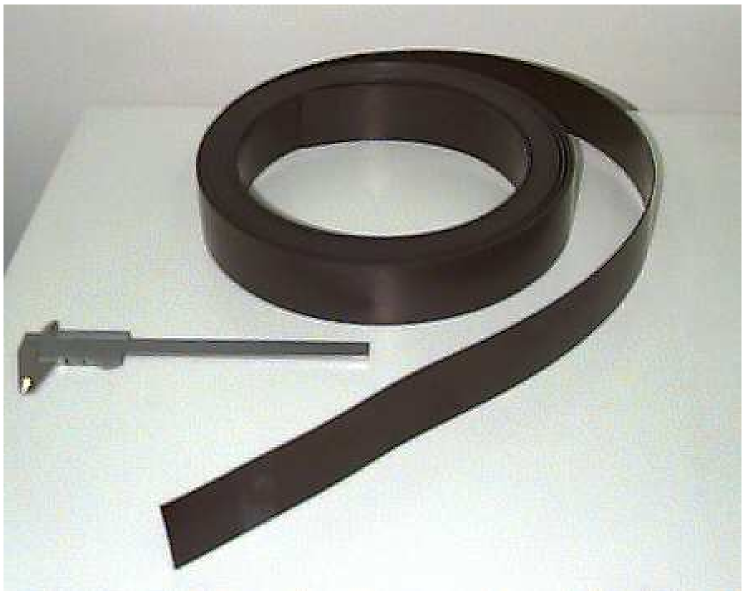

Figure 20: Picture of a 8 m long extruded prototype.

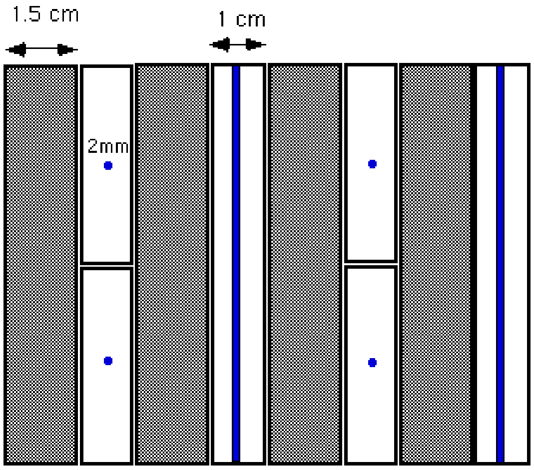

Figure 21: Calorimeter stratigraphy in the crossed scintillator strips option.

7 Photodetectors

The conservative solution of the N^OE calorimeter read out is based on commercially available single PMTs or 16 channel Hamamatsu R 5900 00 M16 multianode photomultiplier with 4 mm $\times$ 4 mm pixel size.

Recently, the technology of multichannel photodetector shad significant improvements. These devices are becoming more and more available and the N^OE calorimeter could benefit of such a superior technology, thus improving the quality of the event pattern. Taken into account reliability, cost and power dissipation, 100k read out channels are the extreme limit in the use of single photomultipliers. For higher numbers, the use of a new high technology multipixel device at lower cost is mandatory.

Two new optical devices will be examinated: hybrid photodiodes (HPD) and multipixel Electron Bombarded CCD (EBCCD).

7.1 HPD's

The HPD tube [22] is a fast device with very simple structure, high linearity and great reliability, made of an ordinary photocathode mounted in front of a semiconductor diode. Between them there is a vacuum gap and they are held at a voltage of few kvolts. An incoming photon is converted on the photocatode into a photoelectron, then accelerated and focused towards a reverse biased silicon diode by an electrostatic focusing system.

Two focusing systems can be used:

- An electro-statically focused HPD, that demagnifies the spherical shaped input photocatode (e.g. 40 mm diameter) to a smaller spot anode (e.g. 11 mm), where the diode is located.

- A proximity focused HPD, with photocatode and diode of identical size active area, separated by a small gap where the electric field is planar and uniform.

In both devices the accelerated photoelectrons bombard the diode generating electron hole pairs gain, proportional to the accelerating voltage. The current can be detected and amplified by a charge amplifier.

Without power consumption, that is a fundamental feature for many channel experiments, the HPD shows high linearity (many orders of magnitude), stability (0.1%), good timing and extremely high photoelectron resolution.

Since the photocathode is imaged onto a silicon chip, by subdividing the silicon diode in pixels, HPD can become a position sensitive device very useful in N^OE to reconstruct the event topology. It is worth remarking that the ability to measure as correctly as possible kinematical and geometrical parameters of the event (energy, coplanarity, direction of the shower axis, etc.) allows to improve the event reconstruction when the τ lepton coming from ν_τ CC is produced in the calorimetric target.

The photoelectron pattern is imaged onto the silicon chip anode with micron accuracy. The silicon diode segmentation is not a limit, since with appropriate bias voltage very little diffusion can occur within the chip, so the HPD position resolution are limited only by the light concentration on the photocatode. Recently, 20-150 pixel tubes are available from the DEP manifacturer.

7.2 Electron Bombarded CCD (EBCCD)

This device consists of an electrostatically focused image intensifier vacuum tube with a backside bombarded thinned silicon pixel array CCD in place of the phosphor screen. Single photoelectron detection capability and inner gain (electron-hole pairs per photoelectron) tunable from 500 to 4000 are achievable. The front end electronics performs fast image read out (10 Mhz clock).

A megapixel Electron Bombarded CCD (EBCCD) has been developed by INFN and Protvino in collaboration with the russian industry Geosphaera. As in HPD device the restriction on the number of channels per EBCCD tube comes from the maximum number of fibers that can be seen by the photocatode. New samples of EBCCD tube with the same features but with a photocatode diameter of 80 mm and an image demagnification of 5 have been designed and are under test.

8 Calorimeter read out

Crossed Fiber Bar Option

In the crossed fiber bar option (Table 1) the calorimeter light signals can be read by classical, reliable and low cost photomultipliers. In 5×5 cm^2 cell segmentation about 20 phe's are produced by a minimum ionizing particle. The good signal features and the number of channels to read, make the single PMT the most safe and convenient solution for this layout.

In this option, for each calorimetric X,Y cell, all the fibers can be grouped together at each side on 3/4 inch R4125 HAMAMATSU PMT's, thus collecting all the light and maximizing the electronic signal. In fact, unless the calorimeter segmentation is further pushed, the end fiber spot to photodetector pixel area ratio could be too large for a multipixel read out solution. As a consequence, the use of multipixel devices (R5900M16 HAMAMATSU PMT or

HPD) needs a Winston cone light concentrator [27] to carefully match up the fiber spot to the multipixel photodetector.

Crossed Fiber Planes Option

In the fiber planes option, the finer X,Y sampling requires more read out channels and the use of multipixel photocatode seems to be mandatory. For each channel, a Winston light concentrator is coupled to a clear fiber ($1 \div 2$ mm) or/and to a demagnifying system, such as electrostatically focusing HPD or EBCCD.

About 1800 HPDs are needed to read the whole calorimeter using 100 pixels tube for $5 \times 5\mathrm{cm}^2$ calorimeter cell (see Table 4).

For the same calorimeter segmentation, assuming a working area of 80 mm photocathode diameter, 180 EBCCD tubes are required to read the whole $N^{O}E$ calorimeter.

In both cases, the very conservative hypothesis of a 2 mm diameter clear fiber has been considered. Using thinner fibers, the number of multipixel devices can be reduced by the square of the fiber diameter. It is worth noting that high density channels/photocatode-area largely reduces the cost per channel making possible high granularity read out. As an example, the use of $1.5 \div 1$ instead of 2 mm fiber diameter, results in a reduction $2 \div 4$ respectively in the number of photodetectors, thus lowering considerably the cost.

Crossed Scintillator Strip Option

Finally, in the crossed scintillator strip option, multipixel readout like EBCCD, HPD and multi-PMT's can be easily implemented: the small WLS fiber ($1 \div 2$ mm of diameter) well matches up the pixel dimension with no need for a light concentrator or demagnifying input diameter tubes (electrostatically focusing HPD). In fact, the physical light collection process automatically determines the end detector/pixel area reduction. However, in this process, a large fraction of photoelectrons are lost, thus making the light signal a bit critical for long size detector (few photoelectrons). Shape of the strip, WLS fiber diameter and reflectivity as well, must be carefully considered in order to optimize the scintillator strip to clean fiber light collection.

Either EBCCD or even proximity focusing HPD without demagnification are the best devices for this calorimeter option. About 2200 HPD are needed to read the whole 1×4 cm^2 calorimeter cells using a 100 pixel tube, or 220 EBCCD 80 mm diameter photocathode tubes.

A 73 pixel has been adopted for the calorimeter read out of the CMS detector.

Calorimeter Option	Photodetector type	Photodetector number	Channels	Estimated cost (M dollars)
CFB CAL 5 × 5 cm^2	H.R4125 single PMT	73 k	73 k	7
	H.R5900 M16 (+ W. cone)	4750	76 k	4
	HPD electr. focus. (+ W. cone)	1500	73 k	3.5
CFP CAL 5 × 5 cm^2	HPD electr. focus. (+ W. cone)	1800	180 k	5
	EBCCD (+ W. cone)	180	180 k	4
	H.R5900 M16 + W. cone	11 k	180 k	8
CSS CAL 4 × 1 cm^2	HPD prox. focus.	2200	220 k	6
	EBCCD	220	220 k	5
	H.R5900 M16	14 k	220 k	9

Table 6: Calorimeter readout features: HPD and EBCCD use 2 mm clear fibers.

In Table 6 the electronic read out system and the relative cost for the different calorimeter options are summarized. In this evaluation, amplifiers, dividers, power supplies, crates, cables and connectors are included.

The HPD and EBCCD device numbers are calculated in the worst case in which 2 mm diameter clear fiber are used. Hence this number could be safely reduced by a factor $2 \div 4$ as described above. A classical 16 multianode PMT solutions is also indicated.

9 Calorimeter simulations

In this section the status of knowledge about the expected performances of the baseline detector implemented with 3 different calorimeter options will be described and compared. By using a GEANT 3.21 based Monte Carlo simulation program, the energy resolution for electron and hadrons has been evaluated. The detector simulation is performed considering:

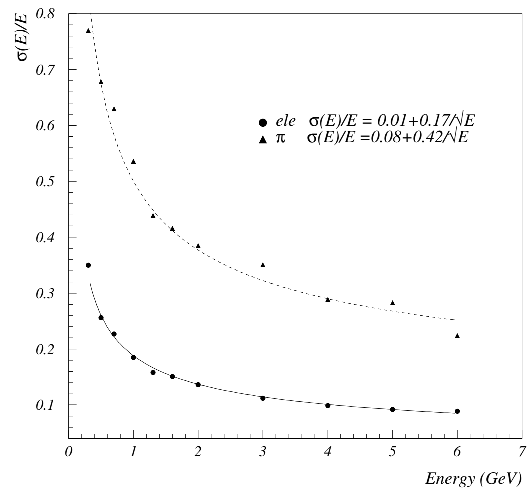

Figure 22: Simulated energy resolutions for electromagnetic and hadronic showers for the CFB calorimeter options.

1. The light produced by the passage of the particles is propagated along the fibers introducing gaussian fluctuation of about 15% around the estimated attenuation length.

2. According to the measured light yield for the mimimum ionizing particle, a mean value of 20 p.e./MeV on each PMT is assumed. As far as the CSS option is concerned, an efficiency ϵ=10% is assumed for trapping inside the fiber the light produced in the scintillator strips. Statistical Poisson fluctuations are applied to the number of primary photo-electrons.

3. The gain of PMTs is assumed equal to $1.5{\cdot}10^7$, with allowed fluctuation of the order of 30%, to take into account both quantum conversion efficiency fluctuation and Poisson fluctuation in the number of secondary electrons extracted.

The electron and pion energy resolutions are shown in Fig. 22, 23 and 24 for crossed bar, crossed fiber and scintillator strip options respectively.

Crossed fiber bar(CFB) and crossed fiber plane(CFP) layouts have similar energy resolution behaviour, since parameters as fiber density, sampling, radiator and interaction length are practically equal.

From these first results, these kinds of scintillating fiber calorimeters seem to allow a valid energy measurement: a good energy resolution is obtained and

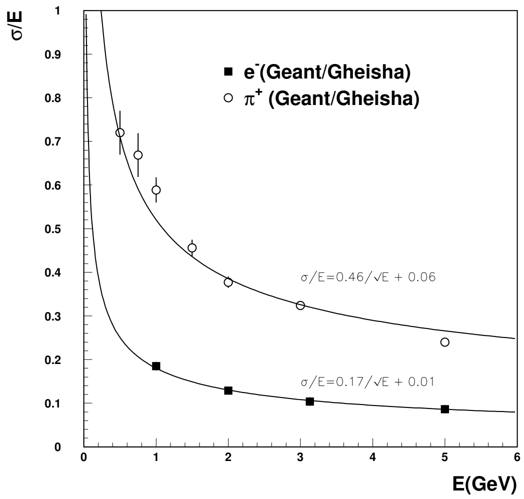

Figure 23: Simulated energy resolutions for electromagnetic and hadronic showers for the CFP calorimeter options.

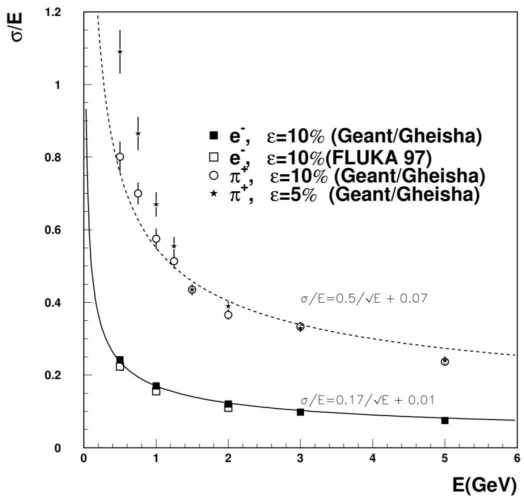

Figure 24: Simulated energy resolutions for electromagnetic and hadronic showers for the CSS calorimeter option.

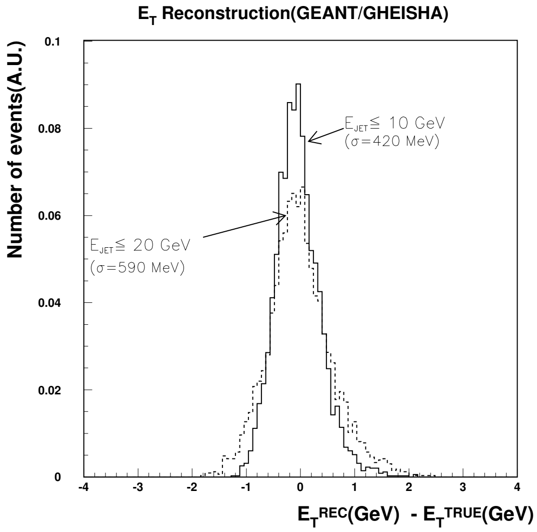

Figure 25: Distribution of the difference between the true and the reconstructed jet transverse energy for the CFP calorimeter option.

it seems possible to obtain almost equal signals for electrons and hadrons of the same energy.

The crossed scintillator strip option (CSS) shows a simulated resolution comparable to that obtainable in the previous fiber layouts. This result is not so difficult to understand: many parameters in the described layout are very similar: the sampling frequency, the absorber material and the density.

The tau identification is based on a kinematical selection: when tau decays, the escaping neutrino(s) will produce some missing momentum and peculiar event angular correlation as well. No missing momentum is expected in the electron and muon neutrino interactions, apart from Fermi motion and nuclear reinteraction. The most important source of "fake" missing momentum in ν_μ,ν_e interactions, comes from the calorimeter performance and neutral particles escaping detection. In Fig. 25 the simulated transverse energy resolution for the crossed fiber planes option is shown. As a comparison in Fig. 26 the same resolution for the crossed scintillator strip calorimeter is reported.

Although the energy resolution of the three calorimeter configurations is roughly the same, it turns out that the most expensive configuration (CFP) represents the best solution as far as the hadronic shower axis determination and the transverse missing energy reconstruction are concerned. These parameters are relevant features to improve the kinematical rejection of ν_τ CC against ν_μ CC ν_e CC.

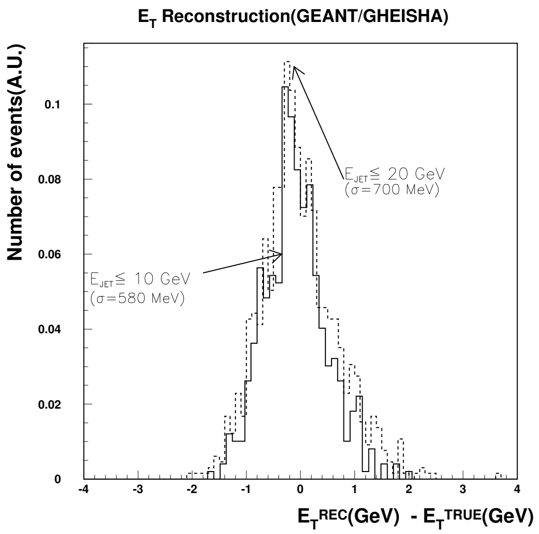

Figure 26: Distribution of the difference between the true and the reconstructed jet transverse energy for the CSS calorimeter option.

The decision about the best calorimeter layout will be made after accurate technical studies concerning mechanical and electronic feasibility and reliability, noise effects on the resolution, and cost. The stability of the performances (energy resolution, shower axis reconstruction, etc.) around the calorimeter equipment working conditions, (performances plateau) has to be the main goal in finalizing the experimental setup.

After a quick look, it turns out that the fiber solution allows to have enough light signal and a proven technique in a layout that has to be optimized from the mechanical point of view. On the other side the strip solution is very interesting for the ease of the construction, but it has to be carefully optimized for the poor light yield.

The $N^{O}E$ R&D program continues, making rapid progresses with the goal to optimize the detection techniques. Detector prototypes have been built and extensively tested. A 2 ton calorimeter and TRD prototype is being built to be exposed to a test beam. Fig. 27 shows a detail of a calorimeter prototype with fibers collected and ready to be coupled to a photodetector.

Considering an exposure of $\sim 1.5 \cdot 10^{20}$ protons on target collected in a few years of running, and the simulated detector performances, the sensitivity limits in the various search channels shown in Fig. 28 will be obtained.

References

1. K.S. Hirata et al. (Kamiokande II Collaboration), *Phys. Lett.* B **280**, 146 (1992)
2. R. Becker-Szendy et al. (IMB Collaboration), *Phys. Rev.* D **46**, 3720 (1992)
3. Y. Suzuki (SuperKamiokande collaboration), Proceedings of the 25th International Cosmic Ray Conference (Durban), (1997)
4. E. Kearns (SuperKamiokande collaboration), presented at TAUP97 (Gran Sasso Laboratories) (1997)
5. P. Bernardini (MACRO Collaboration), Proceedings of 25th International Cosmic Ray Conference (Durban), 7 (1997) 41
6. W.A.Mann et al. (Soudan 2 Collaboration), *Phys. Lett.* B **291**, 200 (1992)
7. Chooz Collaboration, HEP-EX/9711002
8. G. Barbarino et al., "N^OE Atmospheric and long baseline Neutrino Oscillation Experiment", INFN/AE-96/11 (1996)
9. G. Osteria et al., proceedings of the " 7th Pisa meeting on andvanced detector", Isola d' Elba, Italy, May 25-31, 1997.
10. G. Barbarino et al.,"N^OE : A Scintillating Fiber Calorimeter to Search for Long Baseline Neutrino Oscillations", Proceedings of the 25th International Cosmic Ray Conference (Durban), (1997) vol.7 p.101
11. G. Barbarino et al.,"The N^OE detector for a long baseline neutrino oscillation experiment", presented at TAUP97 (Gran Sasso Laboratories) (1997)
12. R. Bellotti et al., *Nucl. Instrum. Methods* A **305**, 192 (1991)
13. E. Barbarito et al., *Nucl. Instrum. Methods* A **365**, 214 (1995)
14. E. Barbarito et al., *Nucl. Instrum. Methods* A **357**, 588 (1995)
15. I. Lehraus et al., *Nucl. Instrum. Methods* A **153**, 347 (1978)
16. D. Buskulic et al., Nucl. Instr. Meth. A 360 (1995) 481
17. T. Ludlam et al., *IEEE Trans. Nucl. Sci.* 28 (1981)
18. E. O'Brien et al., *IEEE Trans.Nucl.Sci.* 40 (1993) 153
19. A. Imanishi et al., *Nucl. Instrum. Methods* A **367**, 244 (1995)
20. Chorus Collaboration, CERN/PPE/93-131 (1993)
21. KLOE Collaboration, LNF 92/019
22. R. DeSalvo et al., *Nucl. Instrum. Methods* A **315**, 375 (1992)
23. G. Martellotti, private communications
24. C. De Marzo et al., *Nucl. Instrum. Methods* **217**, 405 (1983) H. Fessler et al., *Nucl. Instrum. Methods* **228**, 303 (1985) *Nucl. Instrum. Methods* **240**, 284 (1985)

25. M. Adams et al., *Nucl. Instrum. Methods* A **366**, 263 (1995)
26. M. Adams et al., *Nucl. Instrum. Methods* A **378**, 131 (1996)
27. Winston, *Progress in Optics* **27**, 61 (1989)
28. G. Battistoni et al., INFN/AE-03/98 (1998)

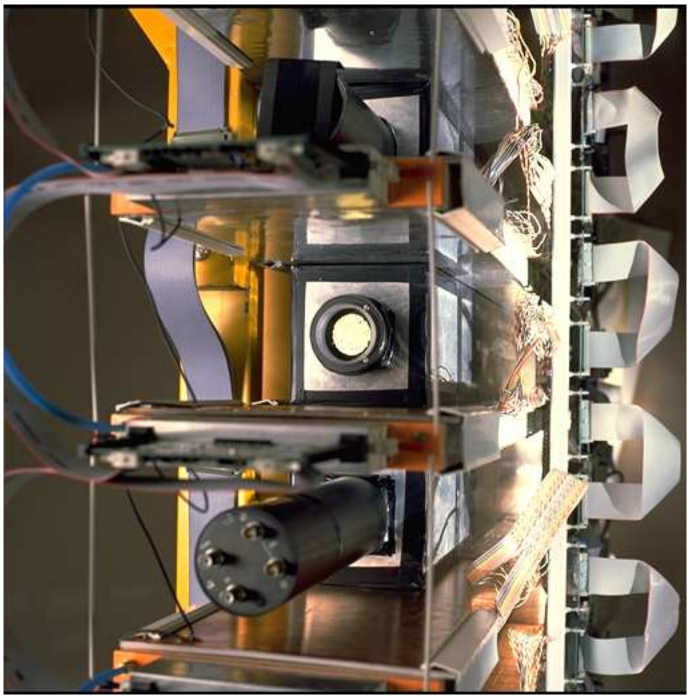

Figure 27: The calorimeter prototype, zoom on the lateral view.

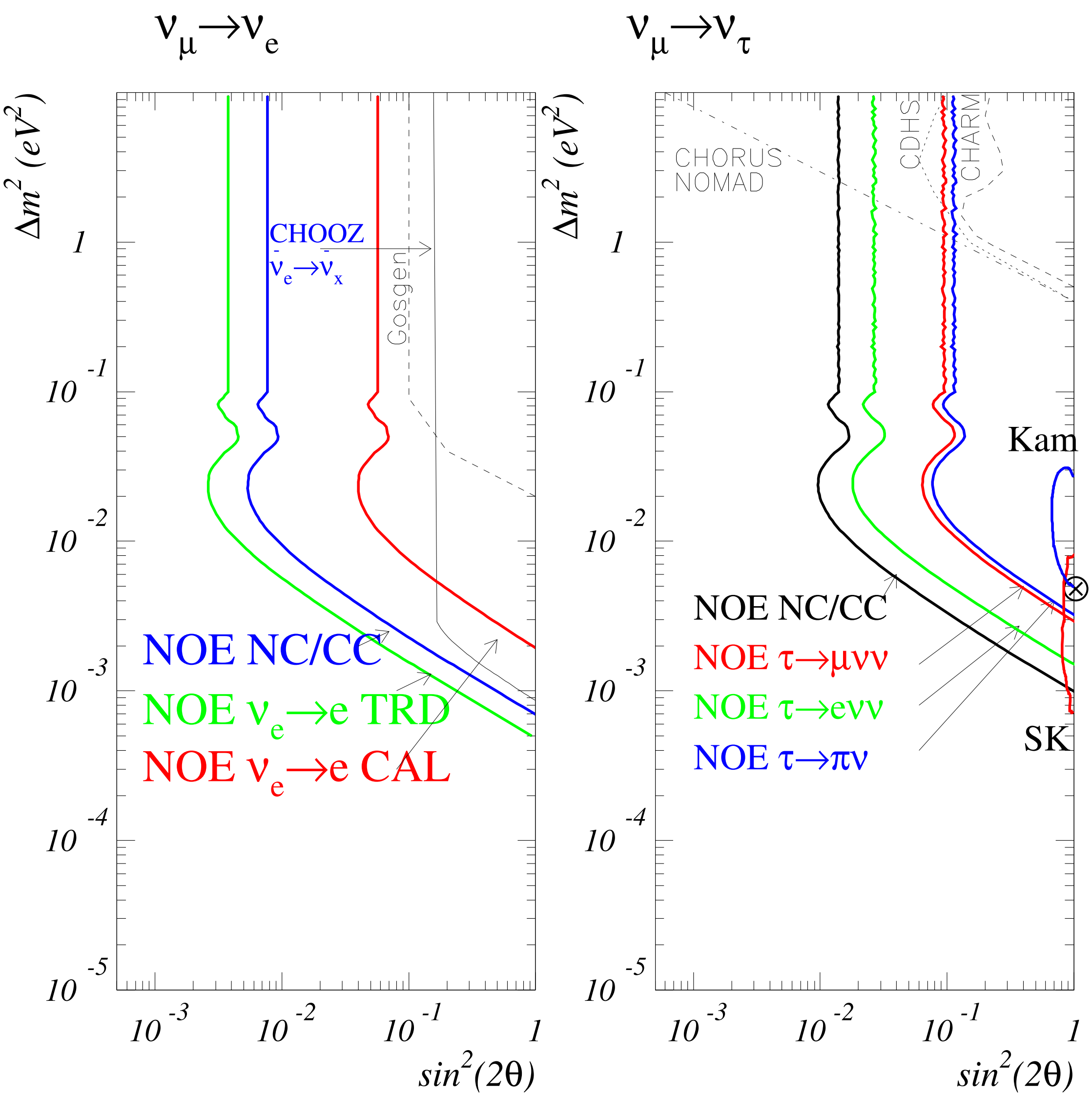

Figure 28: The $N^{O}E$ sensitivity to long baseline ν oscillations